J. Fluid Mech. (2020), *vol.* 893, A18. © The Author(s), 2020.
Published by Cambridge University Press
doi:10.1017/jfm.2020.227

Evolution of a vortex in a strongly stratified shear flow. Part 2. Numerical simulations

Paul Billant[1,†] **and Julien Bonnici**[1]

[1]LadHyX, CNRS, École polytechnique, 91128 Palaiseau CEDEX, France

(Received 20 July 2019; revised 28 January 2020; accepted 17 March 2020)

We conduct direct numerical simulations of an initially vertical Lamb–Oseen vortex in an ambient shear flow varying sinusoidally along the vertical in a stratified fluid. The Froude number F_h and the Reynolds number Re, based on the circulation Γ and radius a_0 of the vortex, have been varied in the ranges: $0.1 \leqslant F_h \leqslant 0.5$ and $3000 \leqslant Re \leqslant 10\,000$. The shear flow amplitude $\hat{U}_S$ and vertical wavenumber $\hat{k}_z$ lie in the ranges: $0.02 \leqslant 2\pi a_0 \hat{U}_S/\Gamma \leqslant 0.4$ and $0.1 \leqslant \hat{k}_z a_0 \leqslant 2\pi$. The results are analysed in the light of the asymptotic analyses performed in Part 1. The vortex is mostly advected in the direction of the shear flow but also in the perpendicular direction owing to the self-induction. The decay of potential vorticity is strongly enhanced in the regions of high shear. The long-wavelength analysis for $\hat{k}_z a_0 F_h \ll 1$ predicts very well the deformations of the vortex axis. The evolutions of the vertical shear of the horizontal velocity and of the vertical gradient of the buoyancy at the location of maximum shear are also in good agreement with the asymptotic predictions when $\hat{k}_z a_0 F_h$ is sufficiently small. As predicted by the asymptotic analysis, the minimum Richardson number never goes below the critical value $1/4$ when $\hat{k}_z a_0 F_h \ll 1$. The numerical simulations show that the shear instability is triggered only when $\hat{k}_z a_0 F_h \gtrsim 1.6$ for sufficiently high buoyancy Reynolds number ReF_h^2. There is also a weak dependence of this threshold on the shear flow amplitude. In agreement with the numerical simulations, the long-wavelength analysis predicts that the minimum Richardson number goes below $1/4$ when $\hat{k}_z a_0 F_h \gtrsim 1.7$ although this is beyond its expected range of validity.

Key words: stratified flows, transition to turbulence, vortex dynamics

1. Introduction

In this paper, we continue the analysis of the evolution of a vortex embedded in a vertically sheared flow in a strongly stratified fluid. The main purpose is to determine the conditions under which the vertical shear can grow sufficiently to lead to the development of the shear instability.

This instability is thought to be an important process for the generation of small scales in stratified flows (Riley & deBruynKops 2003; Laval, McWilliams

† Email address for correspondence: billant@ladhyx.polytechnique.fr

https://doi.org/10.1017/jfm.2020.227 Published online by Cambridge University Press

& Dubrulle 2003; Lindborg 2006; Brethouwer *et al.* 2007). In the case of a columnar counter-rotating vortex pair, Deloncle, Billant & Chomaz (2008) and Waite & Smolarkiewicz (2008) have reported that the vertical shear generated by the zigzag instability can lead to the development of the shear instability. This occurs when the buoyancy Reynolds number $Re_b = ReF_h^2$ (Re is the classical Reynolds number and F_h the horizontal Froude number) is above a threshold since the minimum Richardson number is inversely proportional to Re_b (Riley & deBruynKops 2003; Deloncle *et al.* 2008; Augier & Billant 2011). The subsequent destabilization of the Kelvin–Helmholtz billows leads to small-scale turbulence with spectral characteristics similar to those of randomly forced stratified turbulence (Augier, Chomaz & Billant 2012; Waite 2013).

However, a counter-rotating vortex pair is a very specific flow. Here, we consider the more generic configuration of a single vortex in an ambient shear flow. Such idealized flow contains two elementary ingredients often at play in stratified flows: a horizontal flow with vertical vorticity embedded in a vertical shear flow. In Bonnici & Billant (2020) (referred to hereinafter as Part 1), we have studied such a flow by means of a long-wavelength analysis for $k_zF_h \ll 1$, where k_z is the dimensionless vertical wavenumber of the sinusoidal shear flow. This analysis provides a complete description of the vortex dynamics: the evolution of the vortex axis and angular velocity as well as secondary flows created as the vortex is bent. From these results, we have shown that the minimum Richardson number cannot go below the critical value $1/4$ when $k_zF_h \ll 1$. In the present paper, we will conduct direct numerical simulations (DNS) of this flow for both small and finite k_zF_h and analyse its dynamics in the light of the asymptotic analysis.

The paper is organized as follows. The initial conditions, control parameters and numerical method are described in § 2. An overview of two typical simulations is first given in § 3. Then, the long-wavelength analysis is first briefly summarized in § 4.1 and its predictions for the deformations of the vortex axis are compared to the numerical simulations in § 4.2. We then focus on the evolution of the flow at the vortex centre and the mid-vertical level where the vertical shear is maximum (§ 4.3). Again, the asymptotic analysis is used to rationalize the numerical results. Finally, § 5 concentrates on the evolution of the Richardson number for finite k_zF_h. Section 6 summarizes and discusses the results.

2. Formulation of the problem

2.1. *Initial conditions and governing equations*

As in Part 1, the initial flow is chosen as

$$\boldsymbol{u}(\boldsymbol{x}, t=0) = \boldsymbol{U}_S + \boldsymbol{u}_v, \tag{2.1}$$

where $\boldsymbol{U}_S$ is a sinusoidal shear flow and $\boldsymbol{u}_v$ a columnar vortex with a Lamb–Oseen profile

$$\boldsymbol{U}_S = U_S \sin(k_z z)\boldsymbol{e}_x, \quad \boldsymbol{u}_v = \frac{1-\exp(-r^2)}{r}\boldsymbol{e}_\theta, \tag{2.2a,b}$$

where (x, y, z) and (r, θ, z) are Cartesian and cylindrical coordinates, respectively, $(\boldsymbol{e}_x, \boldsymbol{e}_y, \boldsymbol{e}_z)$ and $(\boldsymbol{e}_r, \boldsymbol{e}_\theta, \boldsymbol{e}_z)$ are the associated unit vectors. The horizontal and vertical velocities in Cartesian coordinates are denoted $\boldsymbol{u}_h = (u, v)$ and w.

In (2.2), the length and time have been non-dimensionalized by the vortex radius a_0 and the turnover time $2\pi a_0^2/\Gamma$ of the vortex, where Γ is the vortex circulation.

https://doi.org/10.1017/jfm.2020.227 Published online by Cambridge University Press

F_h	Re	k_z	U_S	l_z	n_x	n_y	n_z	δt
0.1	6000	π	0.2	2	512	512	256	0.005
0.1	10 000	2	0.2	3.142	512	512	256	0.005
0.1	6000	2	0.4	3.142	512	512	256	0.005
0.5	6000	0.3	0.2	20.94	384	384	448	0.01
0.5	6000	π	0.2	2	832	832	256	0.005
0.5	6000	$3\pi/2$	0.2	1.333	832	832	448	0.005

TABLE 1. Overview of the physical and numerical parameters of some typical simulations. For all simulations, the horizontal dimensions of the domain are $l_x = l_y = 18$.

The shear amplitude U_S and wavenumber k_z are therefore non-dimensional: $U_S = \hat{U}_S 2\pi a_0/\Gamma$, $k_z = \hat{k}_z a_0$, where $\hat{U}_S$ and $\hat{k}_z$ are the corresponding dimensional quantities. The governing equations are the incompressible Navier–Stokes equations under the Boussinesq approximation (see Part 1). The Reynolds, Froude and Schmidt numbers are defined as

$$Re = \frac{\Gamma}{2\pi\nu}, \quad F_h = \frac{\Gamma}{2\pi a_0^2 N}, \quad Sc = \frac{\nu}{\kappa}, \tag{2.3a–c}$$

with ν the viscosity, κ the diffusivity and N the Brunt–Väisälä frequency, which is assumed constant.

2.2. *Numerical method*

The equations are integrated numerically by means of a pseudo-spectral method with periodic boundary conditions and a fourth-order Runge–Kutta time advancement scheme (Deloncle *et al.* 2008). An elliptic truncation of the top one third of the modes in each direction is applied. The viscous and diffusive terms are integrated exactly. The horizontal size of the computational domain is taken large $l_x = l_y = 18$ in order to minimize the effect of the periodic boundary conditions. Periodic boundary conditions are indeed responsible for the presence of image vortices located in the virtual boxes adjacent to the computational domain. The strain field due to these image vortices is proportional to $\Gamma/(2\pi l_x^2)$ and $\Gamma/(2\pi l_y^2)$. Periodic boundary conditions also imply that the net circulation over the domain should be zero (Pradeep & Hussain 2004; Otheguy, Chomaz & Billant 2006). Since a single vortex with a non-zero circulation Γ is simulated here, a small background uniform vertical vorticity $-\Gamma/(l_x l_y)$ is therefore artificially present.

Although these two artefacts could be suppressed by implementing the method proposed by Rennich & Lele (1997), we have chosen to minimize them by simply taking a large box. Several tests with larger boxes (Bonnici 2018) have shown that setting $l_x = l_y = 18$ gives results almost independent of the box size while being not too computationally expensive. The vertical size is set to $l_z = 2\pi/k_z$, so that a single wavelength of the shear flow is simulated.

Table 1 lists the parameters of some typical simulations. The number of grid points in the x and y directions have been varied from $n_x = n_y = 384$ to $n_x = n_y = 832$ depending on the values of the Reynolds and Froude numbers. The number of grid points in the vertical direction ranges from $n_z = 256$ to $n_z = 448$ depending on the values of k_z, Re and F_h. Typically, a high resolution is required for the parameters where the shear instability develops because it generates small billows while a

https://doi.org/10.1017/jfm.2020.227 Published online by Cambridge University Press

moderate resolution is sufficient for the other cases. When k_z increases, the horizontal and vertical resolutions have to be increased also since the vertical gradients are larger. The accuracy of the results has been checked by increasing the resolution or the domain horizontal sizes in several runs. The time step varies from $\delta t = 0.0025$ to $\delta t = 0.01$. All the numerical simulations have been carried out for $Sc = 1$. The Froude number has been always kept below unity so as to remain in the strongly stratified regime. The shear amplitude U_S is also always kept below unity, meaning that the vortex is stronger than the shear flow. The vertical wavenumber has been varied in the range $0.1 \leqslant k_z \leqslant 2\pi$. The Reynolds number has been varied from $Re = 3000$ to $Re = 10\,000$.

3. Overview of the dynamics

3.1. *Qualitative description*

We first begin by a description of two different simulations in order to give an overview of the flow dynamics.

Figures 1 and 2 display the potential vorticity $\Pi = \boldsymbol{\omega} \cdot [\nabla b + 1/F_h^2 \boldsymbol{e}_z]$, where $\boldsymbol{\omega}$ is the vorticity and b the buoyancy, at different times for $k_z = \pi$, $F_h = 0.1$ and $k_z = 3\pi/2$, $F_h = 0.5$, respectively, whereas U_S and Re are fixed to $U_S = 0.2$ and $Re = 6000$. The first column shows three-dimensional contours while the second column represents a corresponding horizontal cross-section at the vertical level $z = l_z/4$. The vortex is mostly displaced in the direction of the shear flow, but also slightly in the perpendicular direction as seen in the horizontal cross-sections. Hence, the vertical plane containing the vortex axis is actually oblique relative to the (x, z) plane. The displacement in the y direction is weaker in figure 1 than in figure 2.

A common feature of both simulations is that the potential vorticity decreases faster in the regions of high shear $z = 0, l_z/2$ than in the regions of weak shear $z = l_z/4, 3l_z/4$ (figures 1*e*, 2*e*,*g*). Thus, the vortex seems to be torn apart into two separate pancake vortices at large times.

Figure 3 displays the corresponding total vertical shear of the horizontal velocity $\sqrt{S_z} = \sqrt{(\partial u/\partial z)^2 + (\partial v/\partial z)^2}$ (colour) in the vertical cross-section at $y = 9$, i.e. passing through the vortex centre at $t = 0$. The superimposed black lines show the total density $\rho_t = -(\rho_0/g)(b + z/F_h^2)$, where ρ_0 is the reference density and g the gravity. For $k_z = \pi$, $F_h = 0.1$ (figure 3*a*,*c*,*e*,*g*), the shear is maximum in the vortex core at the point $x_c = 9$, $z_c = 0, l_z/2$ (note that these coordinates correspond to those of the computational domain where the vortex centre is initially in the middle $x = 9$, $y = 9$). As the vortex is progressively bent, $\sqrt{S_z}$ grows monotonically with time and becomes rapidly much higher than the maximum ambient shear $\max(\sqrt{S_z}) = k_z U_S \simeq 0.6$ (figure 3*a*,*c*,*e*,*g*). The iso-density lines remain nearly flat since the stratification is strong for this case.

Figure 4(*a*) shows that the minimum of the Richardson number (black solid line)

$$Ri = \frac{\dfrac{1}{F_h^2} + \dfrac{\partial b}{\partial z}}{S_z} \tag{3.1}$$

decreases with time from $\min(Ri) = 1/(F_h k_z U_S)^2 = 253$ at $t = 0$ down to $\min(Ri) = 3.7$ at $t = 22$ and then slowly re-increases. The quantity $\min(Ri)$ thus remains well above the critical value $1/4$ necessary for the development of the shear instability of a steady parallel inviscid shear flow (Miles 1961; Howard 1961).

https://doi.org/10.1017/jfm.2020.227 Published online by Cambridge University Press

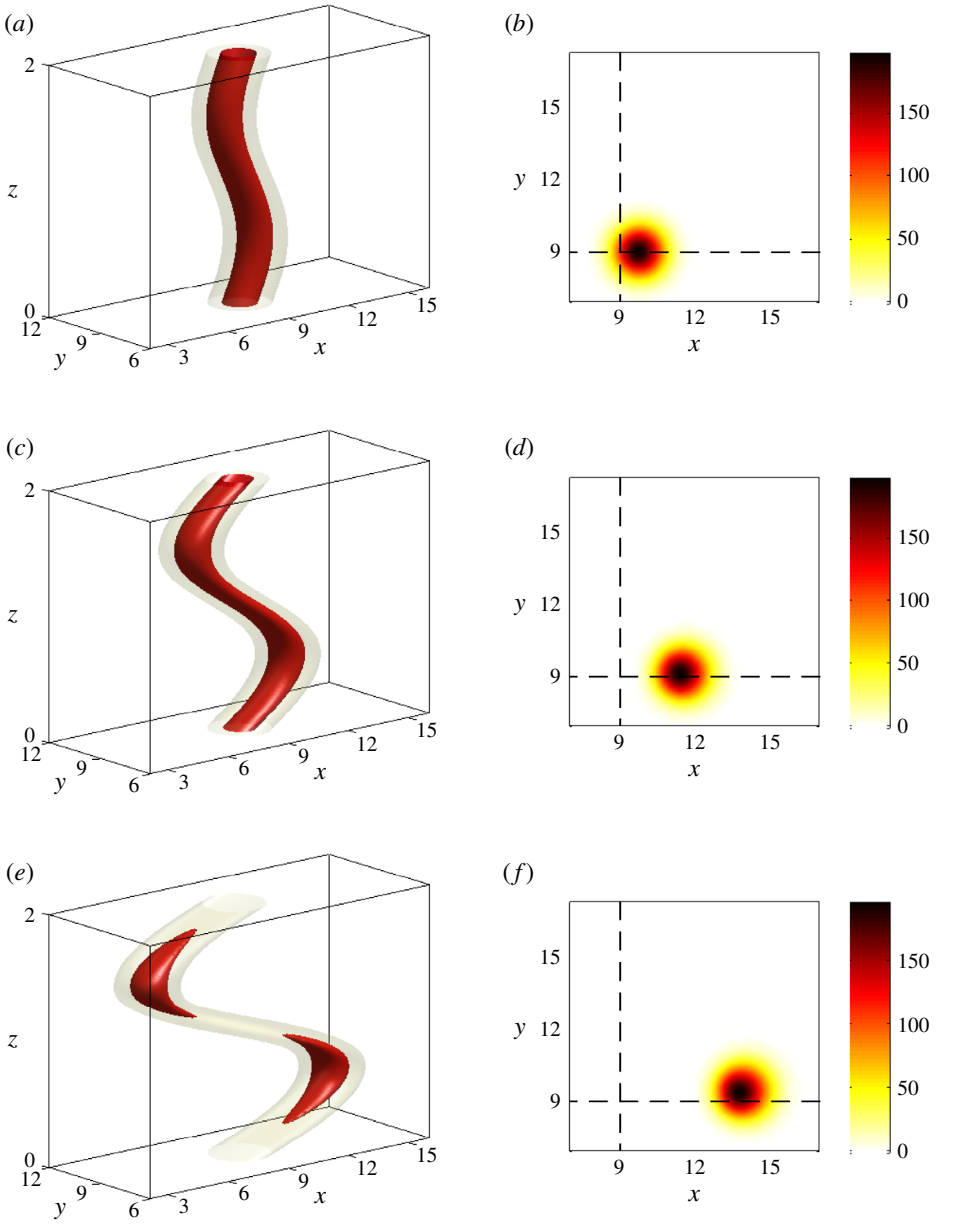


FIGURE 1. (*a*,*c*,*e*) Three-dimensional contours of the potential vorticity at different times for $F_h = 0.1$, $k_z = \pi$, $U_S = 0.2$ and $Re = 6000$. (*b*,*d*,*f*) Corresponding horizontal cross-sections in the plane $z = l_z/4$ where the advection is the most intense. The times shown are (*a*,*b*) $t = 4$, (*c*,*d*) $t = 13$, (*e*,*f*) $t = 26$. In (*a*,*c*,*e*), the isocontours correspond to 20 % (light grey or yellow) and 60 % (dark grey or red) of the initial maximum value.

For $k_z = 3\pi/2$, $F_h = 0.5$ (figure 3*b*,*d*,*f*,*h*), the growth of the maximum shear $\sqrt{S_z}$ is not monotonic. There is a first stage where the shear is very weak within the vortex core (see figure 3*b* at $t = 4$), i.e. the response of the vortex tends to cancel the ambient shear. Then, the vortex becomes tilted as for $k_z = \pi$,

https://doi.org/10.1017/jfm.2020.227 Published online by Cambridge University Press

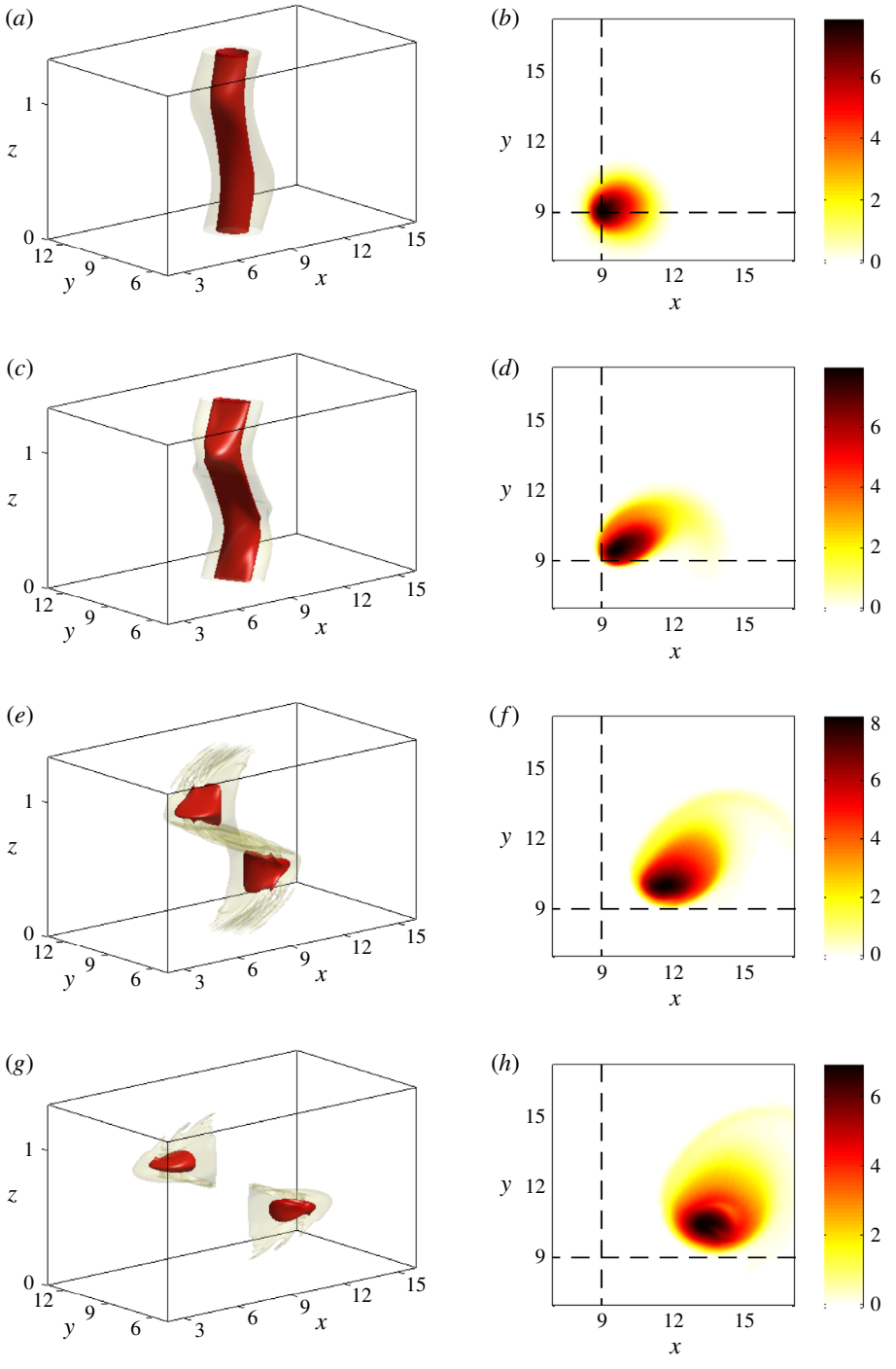


FIGURE 2. Same as figure 1 except that $F_h = 0.5$, $k_z = 3\pi/2$. The times shown are (*a*,*b*) $t = 4$, (*c*,*d*) $t = 13$, (*e*,*f*) $t = 26$, (*g*,*h*) $t = 36$.

https://doi.org/10.1017/jfm.2020.227 Published online by Cambridge University Press

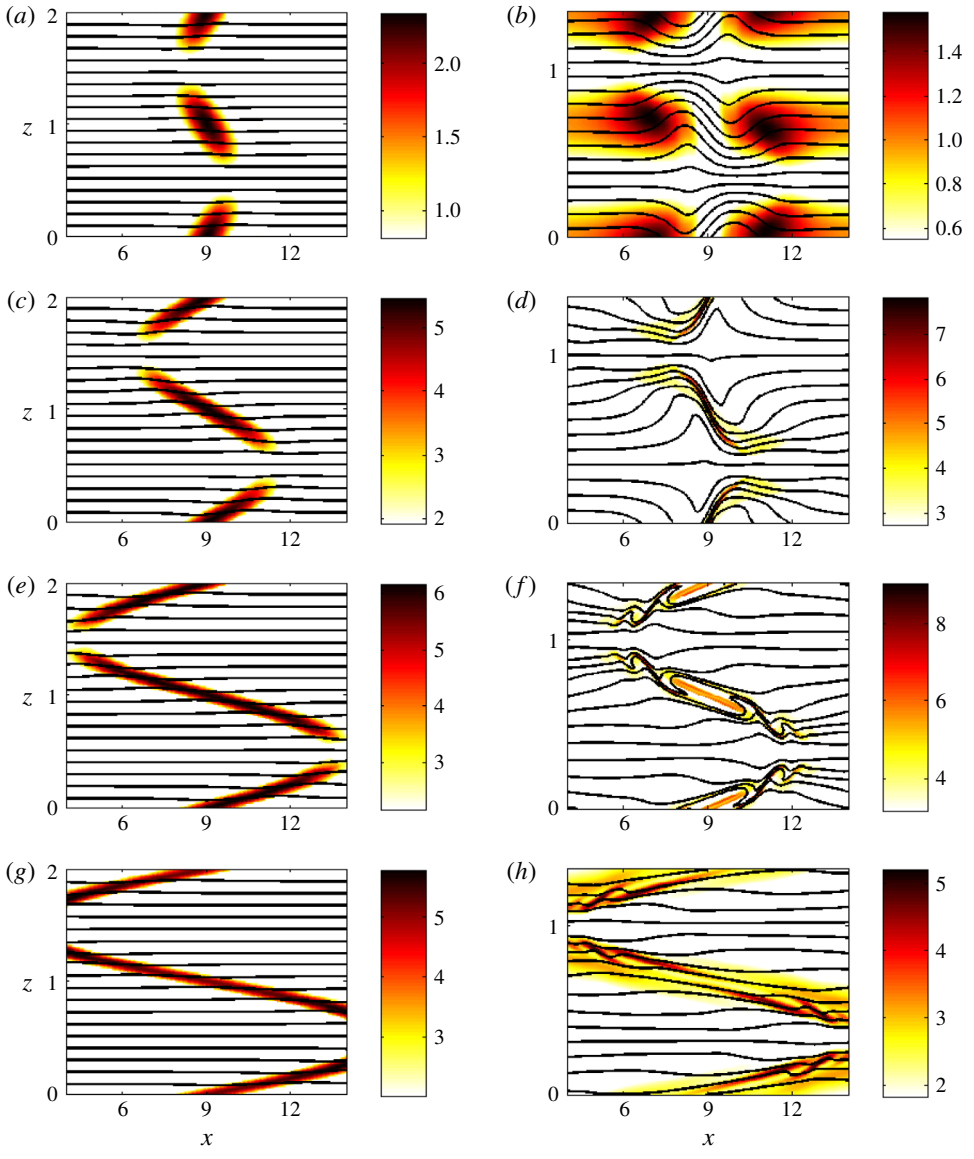


FIGURE 3. Vertical cross-sections of the shear $\sqrt{S_z}$ (colour) and of the total density ρ_t (black contour lines) in the plane $y = 9$, for $F_h = 0.1$, $k_z = \pi$ (a,c,e,g) and $F_h = 0.5$, $k_z = 3\pi/2$ (b,d,f,h), for $U_S = 0.2$ and $Re = 6000$. The times shown are (a,b) $t = 4$, (c,d) $t = 13$, (e,f) $t = 26$, (g,h) $t = 36$.

$F_h = 0.1$, and the maximum shear is encountered in the vicinity of $x_c = 9$, $z_c = 0$, $l_z/2$ (figure 3*d*) with values approximately ten times larger than the ambient maximum shear max $(\sqrt{S_z}) \simeq 0.9$. The regions of high shear are remarkably thin. Later on, the flow strongly dissipates in these regions and the shear becomes maximum at points away from (x_c, z_c) (figure 3*f*,*h*). During this evolution, the iso-density lines are strongly deformed in contrast to $k_z = \pi$, $F_h = 0.1$. Some overturns can even be seen at some locations at $t = 26$ (figure 3*f*). As seen in figure 4(*a*), the minimum Richardson number

https://doi.org/10.1017/jfm.2020.227 Published online by Cambridge University Press

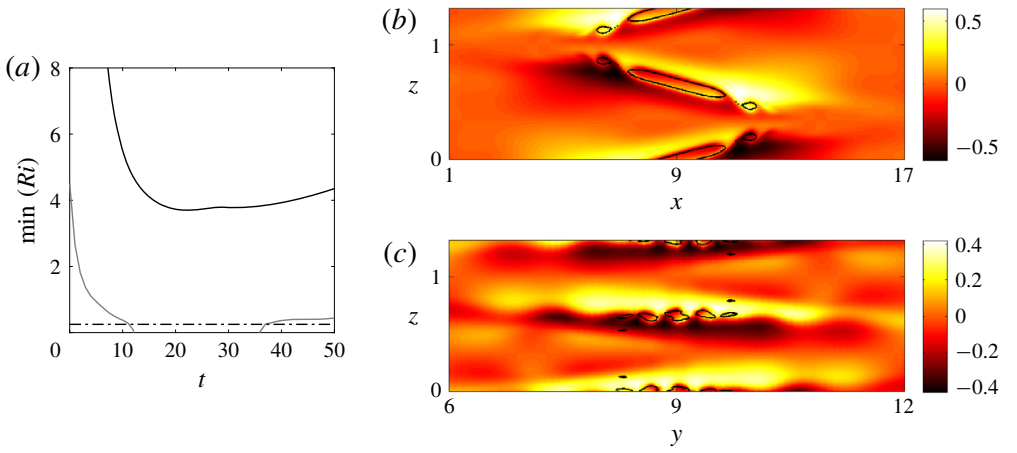


FIGURE 4. (*a*) Minimum Richardson number as a function of time for $U_S = 0.2$, $Re = 6000$ and $F_h = 0.1$, $k_z = \pi$ (black solid line) and $F_h = 0.5$, $k_z = 3\pi/2$ (grey solid line) from the DNS. The horizontal black dash-dotted line shows the critical value $Ri = 0.25$. (*b*,*c*) Vertical cross-sections of the buoyancy b at $t = 26$ in the planes $y = 9$ (*b*) and $x = 9$ (*c*) for $F_h = 0.5$, $k_z = 3\pi/2$, $U_S = 0.2$ and $Re = 6000$. The black contours represent the lines where $Ri = 0.25$.

for this simulation (grey solid line) decreases from $\min(Ri) = 1/(F_h h_z U_S)^2 = 4.5$ at $t = 0$ to a value below $Ri_c = 0.25$ for $11 \leqslant t \leqslant 37$. The (y, z) cross-section at $x = 9$ of the buoyancy at $t = 26$ (figure 4*c*) confirms the presence of Kelvin–Helmholtz billows near $z_c = 0, l_z/2$. In contrast, no billows can be seen in these regions in the corresponding (x, z) cross-section at $y = 9$ (figure 4*b*). This means that the axes of the Kelvin–Helmholtz billows are mostly oriented in the x direction, i.e. they are parallel to the direction of the ambient shear flow. The black contours in figure 4 delineate the regions where $Ri < 0.25$. In addition to the unstable regions near (x_c, z_c), there exist also other unstable regions above and below each pancake vortex at $z = l_z/4$ and $z = 3l_z/4$ as seen in the (x, z) cross-section (figure 4*b*). We can also see some billows and overturns in these regions (figures 4*b* and 3*f*) but in this case, their axes are perpendicular to the direction of the ambient shear. When they occur, these unstable regions appear only in a second stage after those near (x_c, z_c).

3.2. *Time evolution of the vertical shear at the centre*

For $k_z = \pi$, $F_h = 0.1$, the Richardson number is always minimum at the centre point $(x_c = 9, y_c = 9, z_c = l_z/2)$ and at the symmetric point $(x_c = 9, y_c = 9, z_c = 0)$. For $k_z = 3\pi/2$, $F_h = 0.5$, the Kelvin–Helmholtz instability also develops first at these points. It is therefore interesting to investigate the evolution of the vertical shear at these locations.

To this end, we first decompose the flow into a mean flow varying only along the vertical and with time $\bar{\boldsymbol{u}}(z, t)$ and a complementary flow $\boldsymbol{u}^*$

$$\boldsymbol{u} = \bar{\boldsymbol{u}} + \boldsymbol{u}^*, \tag{3.2}$$

https://doi.org/10.1017/jfm.2020.227 Published online by Cambridge University Press

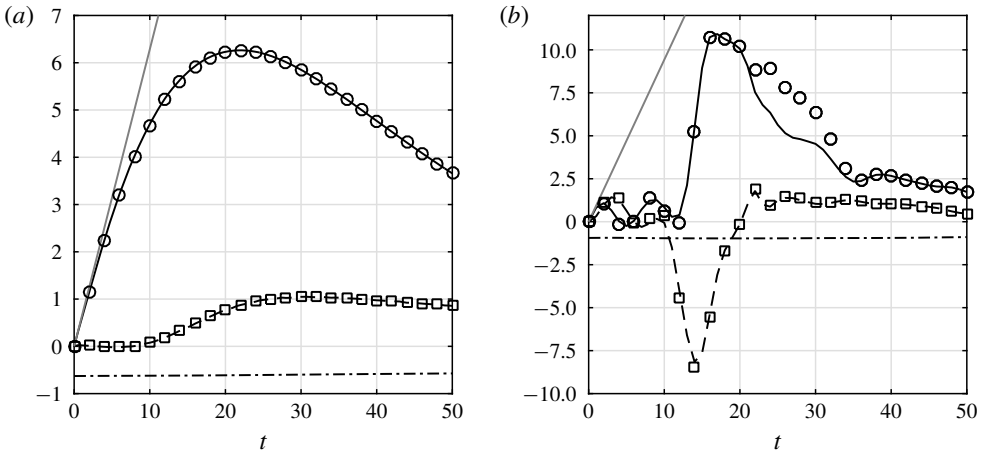


FIGURE 5. Time evolution of $\partial\bar{u}/\partial z$ (black dash-dotted lines), $\partial u^*/\partial z$ (black dashed lines) and $\partial v^*/\partial z$ (black solid lines) at the vortex centre $x_c = 9$, $y_c = 9$, $z_c = l_z/2$ for (*a*) $F_h = 0.1$, $k_z = \pi$, and (*b*) $F_h = 0.5$, $k_z = 3\pi/2$ for $U_S = 0.2$ and $Re = 6000$. The straight grey lines represent the relation $k_z U_S t$. The symbols show the horizontal vorticity components $-\omega_x^*$ (circles) and ω_y^* (squares).

where the overbar denotes the horizontal average over the computational domain, which for any quantity q is defined as

$$\bar{q} = \frac{1}{l_x l_y} \int_0^{l_y} \int_0^{l_x} q(x, y, z, t)\, \mathrm{d}x\, \mathrm{d}y. \tag{3.3}$$

At $t = 0$, we have $\bar{\boldsymbol{u}} = \boldsymbol{U}_S$ and $\boldsymbol{u}^* = \boldsymbol{u}_v$ so that $\bar{\boldsymbol{u}}$ and $\boldsymbol{u}^*$ will be called 'shear flow' and 'vortex flow', respectively.

Figure 5(*a*) shows the evolution of the different shear components $\partial\bar{u}/\partial z$, $\partial u^*/\partial z$ and $\partial v^*/\partial z$ at the centre $(x_c = 9, y_c = 9, z_c = l_z/2)$ for $F_h = 0.1$, $k_z = \pi$, $U_S = 0.2$ and $Re = 6000$. The quantity $\partial\bar{v}/\partial z$ is always equal to zero at the centre and is not plotted. More generally, $\partial\bar{v}/\partial z$ always remains very small at any vertical position compared to $\partial\bar{u}/\partial z$. We see that the mean shear $\partial\bar{u}/\partial z$ (dash-dotted line) remains almost constant and equal to $-k_z U_S = -0.63$. In contrast, the shear component $\partial v^*/\partial z$ (solid line) grows first linearly and then saturates at $t \simeq 22$ at the value $\partial v^*/\partial z = 6.3$, i.e. ten times the ambient shear $|\partial\bar{u}/\partial z|$. The other component $\partial u^*/\partial z$ remains very weak up to $t = 10$ and then increases up to $\partial u^*/\partial z \simeq 1$ at $t = 30$. This quantity therefore saturates at a lower value and later than its counterpart $\partial v^*/\partial z$.

The initial behaviour of the vertical shear of the vortex $\partial u^*/\partial z$ and $\partial v^*/\partial z$ can be simply understood by considering that the vortex is displaced at the velocity $U(z)$ in the x direction, i.e. $\boldsymbol{u}_v(x - Ut, y)$, as assumed by Lilly (1983). This gives

$$\frac{\partial \boldsymbol{u}_v}{\partial z} = -\frac{\mathrm{d}U}{\mathrm{d}z} t \frac{\partial \boldsymbol{u}_v}{\partial x}. \tag{3.4}$$

Since $\boldsymbol{u}_v = (-\Omega y, \Omega x)$, where $\Omega(r)$ is the angular velocity of the vortex, we have $\partial v_v/\partial x = \Omega = 1$ and $\partial u_v/\partial x = 0$ at the centre $r = 0$. Thus, (3.4) yields

$$\frac{\partial u_v}{\partial z} = 0, \quad \frac{\partial v_v}{\partial z} = k_z U_S t, \tag{3.5a,b}$$

https://doi.org/10.1017/jfm.2020.227 Published online by Cambridge University Press

at $z = l_z/2$. The straight grey line in figure 5(*a*) confirms that $\partial v^*/\partial z$ increases initially at the rate $k_z U_S t$. This also explains why $\partial u^*/\partial z$ remains very small initially. The subsequent evolutions will be explained later thanks to the asymptotic analysis performed in Part 1.

In figure 5(*a*), we have also plotted with symbols the horizontal vorticity components $-\omega_x^*$ and ω_y^* where $\boldsymbol{\omega}^* = \boldsymbol{\nabla} \times \boldsymbol{u}^*$. They are nearly superposed to $\partial v^*/\partial z$ and $\partial u^*/\partial z$, respectively, because the vertical velocity is very small compared with the horizontal velocity. In other words, $\omega_x^* \simeq -\partial v^*/\partial z$ and $\omega_y^* \simeq \partial u^*/\partial z$.

Similarly, figure 5(*b*) displays the time evolution of $\partial \bar{u}/\partial z$, $\partial u^*/\partial z$ and $\partial v^*/\partial z$ at the centre point for $F_h = 0.5$ and $k_z = 3\pi/2$, still for $U_S = 0.2$ and $Re = 6000$. In contrast to the case $F_h = 0.1$, $k_z = \pi$ (figure 5*a*), $\partial v^*/\partial z$ follows the relation (3.5) only at the very beginning $t \lesssim 2$. Instead, both shear components $\partial u^*/\partial z$ and $\partial v^*/\partial z$ first oscillate with a phase lag and with a period around 2π, i.e. the period corresponding to the angular velocity on the vortex axis $\Omega = 1$. Because of these oscillations, we can notice that $\partial v^*/\partial z$ goes back to zero around $t \simeq 4$–5 while $\partial u^*/\partial z$ is approximately opposite to $\partial \bar{u}/\partial z$. Thus, the total shear S_z is weak at the centre as already observed in figure 3(*b*) at $t = 4$.

Then, $\partial u^*/\partial z$ and $\partial v^*/\partial z$ are both abruptly amplified up to an absolute value around 10. Remarkably, $\partial u^*/\partial z$ becomes now negative and saturates earlier than $\partial v^*/\partial z$. Later on, $|\partial u^*/\partial z|$ decreases very quickly while $|\partial v^*/\partial z|$ decays more slowly. The vorticity components $-\omega_x^*$ and ω_y^* have been also plotted in figure 5(*b*). They are again almost identical to $\partial v^*/\partial z$ and $\partial u^*/\partial z$ except $-\omega_x^*$ for $21 \leqslant t \leqslant 35$. This corresponds to the time interval when the Kelvin–Helmholtz billows exist. They produce a finite vertical velocity w^*, making the term $\partial w^*/\partial y$ in ω_x^* no longer negligible. In contrast, the term $\partial w^*/\partial x$ is still negligible in ω_y^*, most probably because the axes of the Kelvin–Helmholtz billows are aligned with the x direction.

3.3. *Global energy and enstrophy evolutions*

Figure 6 presents the evolutions of the energies integrated over the whole computational domain for the two simulations for $k_z = \pi$, $F_h = 0.1$, and $k_z = 3\pi/2$, $F_h = 0.5$, previously described. The kinetic energies have been decomposed into a mean part and a vortex part using the decomposition (3.2)

$$\bar{E}_k = \frac{1}{l_z}\int_V \frac{\bar{\boldsymbol{u}}^2}{2}\mathrm{d}V, \quad E_{kh}^* = \frac{1}{l_z}\int_V \frac{\boldsymbol{u}_h^{*2}}{2}\mathrm{d}V, \quad E_{kz}^* = \frac{1}{l_z}\int_V \frac{w^{*2}}{2}\mathrm{d}V, \tag{3.6a–c}$$

where E_{kh}^* and E_{kz}^* are the horizontal and vertical kinetic energies of the vortex part. The integral over the computational domain V is divided by l_z in order to enable the comparisons between simulations carried out with distinct vertical wavelengths (Note that we do not divide by V in order to be able to compare simulations with different horizontal domain sizes). Similarly, the global potential energy per vertical length unit is

$$E_p = \frac{1}{l_z}\int_V \frac{F_h^2 b^2}{2}\mathrm{d}V. \tag{3.7}$$

The kinetic energy of the mean flow $\bar{E}_k$ (black dash-dotted lines) remains approximately constant even if it increases slightly at the beginning for $k_z = 3\pi/2$, $F_h = 0.5$ (figure 6*b*). In contrast, the horizontal kinetic energy of the vortex E_{kh}^* (black dashed lines) decreases regularly following an approximately linear trend. The vertical kinetic

https://doi.org/10.1017/jfm.2020.227 Published online by Cambridge University Press

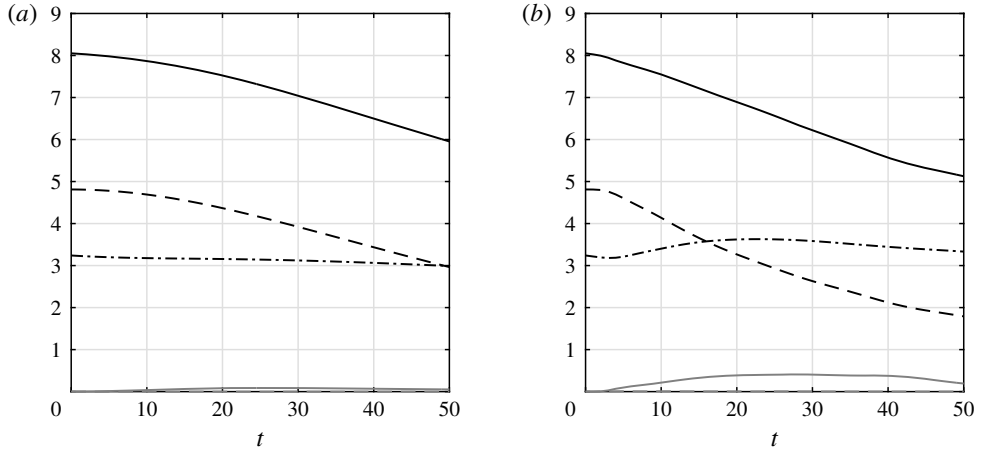


FIGURE 6. Time evolutions of the global kinetic energy $\bar{E}_k + E^*_{kh} + E^*_{kz}$ (black solid line), the mean flow kinetic energy $\bar{E}_k$ (black dash-dotted line), the vortex horizontal kinetic energy E^*_{kh} (black dashed line), the vortex vertical kinetic energy E^*_{kz} (grey dashed line) and the potential energy E_p (grey solid line) for (*a*) $F_h = 0.1$, $k_z = \pi$ and (*b*) $F_h = 0.5$, $k_z = 3\pi/2$ for $U_S = 0.2$, $Re = 6000$.

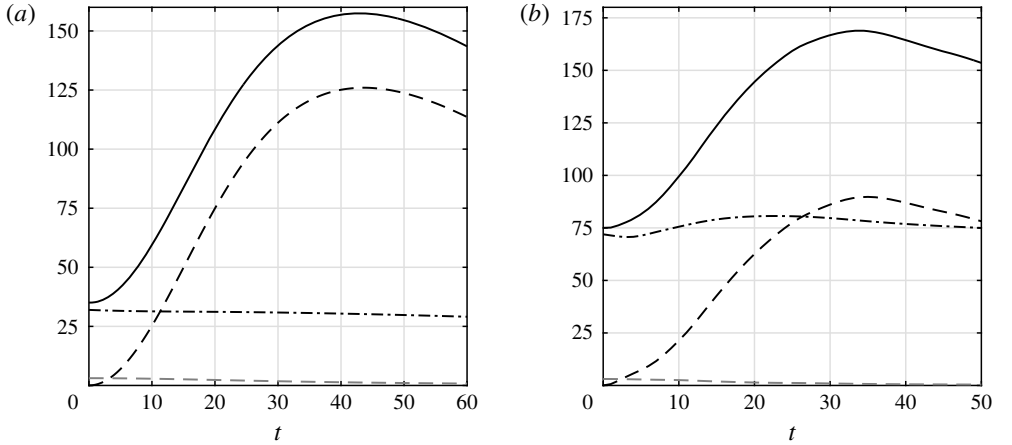


FIGURE 7. Time evolutions of the global total enstrophy $\bar{Z} + Z^*_h + Z^*_z$ (black solid line), the mean flow enstrophy $\bar{Z}$ (black dash-dotted line), the vortex horizontal enstrophy Z^*_h (black dashed line) and the vortex vertical enstrophy Z^*_z (grey dashed line) for (*a*) $F_h = 0.1$, $k_z = \pi$ and (*b*) $F_h = 0.5$, $k_z = 3\pi/2$ for $U_S = 0.2$, $Re = 6000$.

energy E^*_{kz} (grey dashed lines) and the potential energy E_p (grey solid lines) remain always very weak compared with the horizontal kinetic energy.

Likewise, figure 7 displays the evolutions of the global enstrophies per vertical length unit, decomposed using (3.2)

$$\bar{Z} = \frac{1}{l_z}\int_V \frac{\bar{\boldsymbol{\omega}}^2}{2}\mathrm{d}V, \quad Z^*_h = \frac{1}{l_z}\int_V \frac{\boldsymbol{\omega}^{*2}_h}{2}\mathrm{d}V, \quad Z^*_z = \frac{1}{l_z}\int_V \frac{\zeta^{*2}}{2}\mathrm{d}V, \tag{3.8a–c}$$

https://doi.org/10.1017/jfm.2020.227 Published online by Cambridge University Press

where $\bar{\boldsymbol{\omega}}$ is the vorticity of the shear flow and $\boldsymbol{\omega}_h^*$ and ζ^* the horizontal and vertical vorticities of the vortex part. The global horizontal enstrophy of the vortex Z_h^* (black dashed lines) increases and then decreases while its vertical counterpart Z_z^* (grey dashed lines) continuously decays. Remarkably, the growth of Z_h^* is much more pronounced for $k_z = \pi$, $F_h = 0.1$ than for $k_z = 3\pi/2$, $F_h = 0.5$ although the vertical wavenumber k_z is higher in this second case. The enstrophy of the mean shear $\bar{Z}$ remains approximately constant like the mean kinetic energy $\bar{E}_k$. Since the mean enstrophy $\bar{Z}$ for $k_z = 3\pi/2$ is more than twice the one for $k_z = \pi$, the maximum of the total enstrophy (solid lines) is comparable in the two simulations even if max (Z_h^*) is lower for $k_z = 3\pi/2$.

4. Comparison with the long-wavelength asymptotic analysis

4.1. *Reminder*

In Part 1, we have performed a long-wavelength asymptotic analysis for $k_z F_h \ll 1$, i.e. for small vertical Froude number $F_v = k_z F_h = \Gamma/(a_0 l_z N)$. Leading-order viscous effects have been also taken into account. This analysis has provided evolution equations for the position of the vortex centre at each level z

$$\Delta x = U(z)t + \delta x(z,t), \tag{4.1}$$

$$\Delta y = \delta y(z,t), \tag{4.2}$$

where

$$\frac{\partial \delta x}{\partial t} = \left[\frac{\mathcal{A}(z,t)}{2}\frac{\partial^2 \delta y}{\partial z^2} - \left(\vartheta(z,t) + \frac{\partial \mathcal{C}_w}{\partial t}(z,t)\right)\frac{\mathrm{d}^2 U}{\mathrm{d}z^2}\right] F_h^2, \tag{4.3}$$

$$\frac{\partial \delta y}{\partial t} = -\left[\frac{\partial}{\partial z}\left(\frac{\mathcal{A}(z,t)}{2} t \frac{\mathrm{d}U}{\mathrm{d}z}\right) + \frac{\mathcal{A}(z,t)}{2}\frac{\partial^2 \delta x}{\partial z^2} + \frac{\partial \mathcal{S}_w}{\partial t}(z,t)\frac{\mathrm{d}^2 U}{\mathrm{d}z^2}\right] F_h^2, \tag{4.4}$$

where $\mathcal{C}_w$ and $\mathcal{S}_w$ are the effects of internal waves excited at $t = 0$ and that decay quickly afterwards. The parameters $\mathcal{A}$ and ϑ correspond to the self-induction of the vortex and an advection correction, respectively. The expressions of all these parameters are given in Part 1.

An approximation for the solution of (4.3)–(4.4) has been found in Part 1 in the form

$$\delta x = -F_h^2\left[\mathcal{C}_w(z,t) + \int_0^t \vartheta(z,\upsilon)\,\mathrm{d}\upsilon\right]\frac{\mathrm{d}^2 U}{\mathrm{d}z^2}, \tag{4.5}$$

$$\delta y = -F_h^2\left[\mathcal{S}_w(z,t)\frac{\mathrm{d}^2 U}{\mathrm{d}z^2} + \int_0^t \frac{\partial}{\partial z}\left(\frac{\mathcal{A}(z,\upsilon)}{2}\frac{\mathrm{d}U}{\mathrm{d}z}\right)\upsilon\,\mathrm{d}\upsilon\right]. \tag{4.6}$$

In addition, the asymptotic analysis has shown that the angular velocity of the vortex evolves according to

$$\frac{\partial \Omega}{\partial t} = \left[-F_h^2 t\Omega^3 + \frac{t^2}{2Re\tilde{r}}\frac{\partial \zeta_0}{\partial \tilde{r}}\right]\left(\frac{\mathrm{d}U}{\mathrm{d}z}\right)^2, \tag{4.7}$$

where $\zeta_0 = (1/\tilde{r})\partial \tilde{r}^2 \Omega/\partial \tilde{r}$ is the vertical vorticity and $\tilde{r}$ is the local radius with respect to the centre of the vortex at the level z: $\tilde{r}^2 = (x - U(z)t - \delta x)^2 + (y - \delta y)^2$.

https://doi.org/10.1017/jfm.2020.227 Published online by Cambridge University Press

The first term on the right-hand side of (4.7) ensures the conservation of potential vorticity while the second term describes the leading viscous effect. This effect is proportional to t^2 because the vertical shear grows like $t\,\mathrm{d}U/\mathrm{d}z$ at leading order. Internal waves have been neglected in (4.7) since their effects have been shown to be very weak. In Part 1, the equation (4.7) has been solved asymptotically. In particular, an analytic expression for the angular velocity on the vortex axis has been obtained

$$\Omega(\tilde{r}=0,z,t)=\frac{1}{\sqrt{(1+2\gamma T^3/3)^2+T^2}}, \tag{4.8}$$

where $T=F_h t|\mathrm{d}U/\mathrm{d}z|$ and $\gamma(z)=1/(ReF_h^3|\mathrm{d}U/\mathrm{d}z|)$. This expression is in very good agreement with the exact result obtained by numerical integration of (4.7). It will be therefore used in the following.

In addition, the asymptotic analysis has provided the horizontal velocity at order $O[(k_zF_h)^2]$ and the vertical velocity and buoyancy at leading order. They allowed us to predict the evolution of the vertical shear of the horizontal velocity, the vertical buoyancy gradient and the Richardson number at the vortex centre at $z=l_z/2$. These predictions will be compared with the DNS in § 4.3. Before, we begin by presenting in the next section a comparison between the location of the vortex centre observed in the DNS and the asymptotic predictions (4.1)–(4.2).

4.2. *Deformations of the vortex axis*

In order to estimate the position of the vortex centre in the numerical simulations, we have used two methods: one based on the potential vorticity Π and the other on the vertical vorticity ζ. In each case, the displacements of the vortex centre have been estimated from vorticity centroids

$$\Delta x_c^{\Pi}(z,t)=\frac{\langle x\Pi\rangle_h}{\langle\Pi\rangle_h},\qquad \Delta y_c^{\Pi}(z,t)=\frac{\langle y\Pi\rangle_h}{\langle\Pi\rangle_h}, \tag{4.9a,b}$$

or

$$\Delta x_c^{\zeta}(z,t)=\frac{\langle x\zeta\rangle_h}{\langle\zeta\rangle_h},\qquad \Delta y_c^{\zeta}(z,t)=\frac{\langle y\zeta\rangle_h}{\langle\zeta\rangle_h}, \tag{4.10a,b}$$

where the brackets denote

$$\langle\varphi\rangle_h=\int_{\varphi>\varphi_c}\varphi\,\mathrm{d}x\,\mathrm{d}y. \tag{4.11}$$

The horizontal integration is carried out only in the regions where the vorticity is larger than a critical value Π_c, ζ_c. In this way, we exclude the small background vorticity due to the fact that the total vorticity is zero owing to the use of periodic boundary conditions. The values $\Pi_c=0.05\,\max_{t=0}(\Pi)$ and $\zeta_c=0.05\,\max_{t=0}(\zeta)$ have been chosen as they provide results almost independent of the size of the computational domain and the particular values of the thresholds.

The tracking method based on the potential vorticity seems more natural since it is a transported quantity in the inviscid limit. However, we shall see that the method based on the vertical vorticity will enable a closer comparison to the asymptotic results. This is because the condition used to normalize the streamfunction at first order ψ_1 in the asymptotic analysis: $\langle x\nabla_h^2\psi_1\rangle_h=0$, $\langle y\nabla_h^2\psi_1\rangle_h=0$, implies

$$\Delta x_c^{\zeta}=\frac{\langle x\zeta\rangle_h}{\langle\zeta\rangle_h}=\frac{\langle x[\zeta_0+(k_zF_h)^2\nabla_h^2\psi_1+\cdots]\rangle_h}{\langle\zeta_0+(k_zF_h)^2\nabla_h^2\psi_1+\cdots\rangle_h}=\frac{\langle x\zeta_0(\tilde{r})\rangle_h}{\langle\zeta_0\rangle_h}=\Delta x, \tag{4.12}$$

https://doi.org/10.1017/jfm.2020.227 Published online by Cambridge University Press

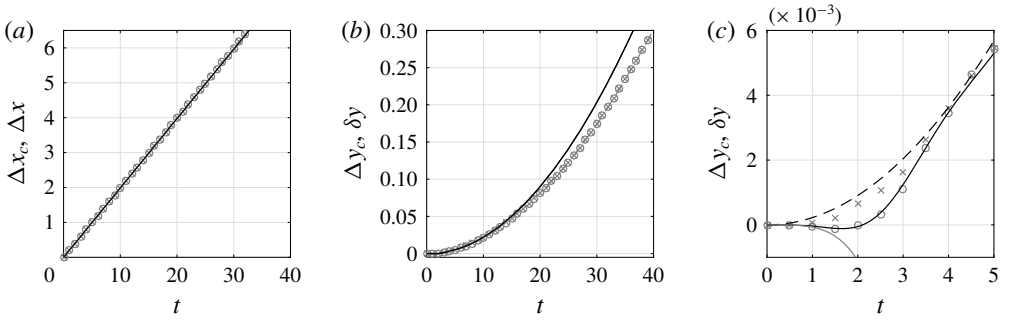


FIGURE 8. (*a*,*b*) Comparison between the vertical vorticity centroids Δx_c^{ζ} and Δy_c^{ζ} (grey open circles), the potential vorticity centroids Δx_c^{Π} and Δy_c^{Π} (grey crosses) and the asymptotic predictions for the displacements Δx and δy (black solid lines) in the plane $z = l_z/4$. (*c*) Displays a close-up view of the initial evolution of Δy_c^{ζ} (grey open circles), Δy_c^{Π} (grey crosses) and δy (black solid line). The asymptotic prediction in the absence of internal waves, i.e. by setting $\mathcal{C}_w = \mathcal{S}_w = 0$ in (4.5)–(4.6) has been also reported (black dashed line). The short-time asymptotic prediction for δy has been plotted as well (grey solid line). The parameters are $F_h = 0.5$, $k_z = 0.3$, $U_S = 0.2$ and $Re = 6000$.

and, similarly $\Delta y_c^{\zeta} = \Delta y$, where $(\Delta x, \Delta y)$ are the asymptotic displacements (4.1)–(4.2) and ζ_0 is the leading-order vertical vorticity.

In the next sections, we compare the asymptotic and numerical results for different parameters.

4.2.1. *In-depth analysis of a simulation*

Figure 8 compares the total displacements $\Delta x = U_S t + \delta x$ and δy as predicted by the asymptotics to the positions Δx_c and Δy_c of the vortex estimated from the vertical vorticity and potential vorticity centroids at the level $z = l_z/4$ for $F_h = 0.5$, $k_z = 0.3$, $U_S = 0.2$ and $Re = 6000$. The agreement is excellent at all times for Δx and up to $t \simeq 15$ for δy. The dominant displacement is in the x direction (figure 8*a*) and given by $U_S t$ while the deviations δx and δy are much smaller.

The displacement of the vortex estimated from the vertical vorticity, $(\Delta x_c^{\zeta}, \Delta y_c^{\zeta})$, and from the potential vorticity, $(\Delta x_c^{\Pi}, \Delta y_c^{\Pi})$, are almost equal. However, if we focus on the initial evolution of Δy_c^{ζ} and Δy_c^{Π} (figure 8*c*), we see that they are actually different for $t \leqslant 4$. The displacement Δy_c^{ζ} (open circles) is first slightly negative for $t \leqslant 2$ in excellent agreement with the asymptotic prediction δy (black solid line). In contrast, the y displacement estimated from the potential vorticity Δy_c^{Π} (crosses) increases monotonically. As explained above, the estimation of the vortex centre from the vertical vorticity is in much better agreement with the asymptotics than the estimation from the potential vorticity because the normalization condition used in the asymptotic analysis is based on the vertical vorticity.

Nevertheless, if the effects of the internal waves are neglected in (4.5)–(4.6) (i.e. $\mathcal{C}_w = \mathcal{S}_w = 0$), the asymptotic prediction (black dashed line) is then close to Δy_c^{Π}. This confirms that internal waves play a key role at the start-up of the flow evolution. Because of these waves, the initial evolution of δy at $z = l_z/4$ is of the form $\delta y = k_z^2 U_S \sigma t^4$, where $\sigma = -3.826 \times 10^{-3}$ is a constant (Part 1), as shown by the grey solid line in figure 8(*c*). In contrast, when internal waves are neglected, δy evolves initially as $\delta y \propto t^2$ (black dashed line).

https://doi.org/10.1017/jfm.2020.227 Published online by Cambridge University Press

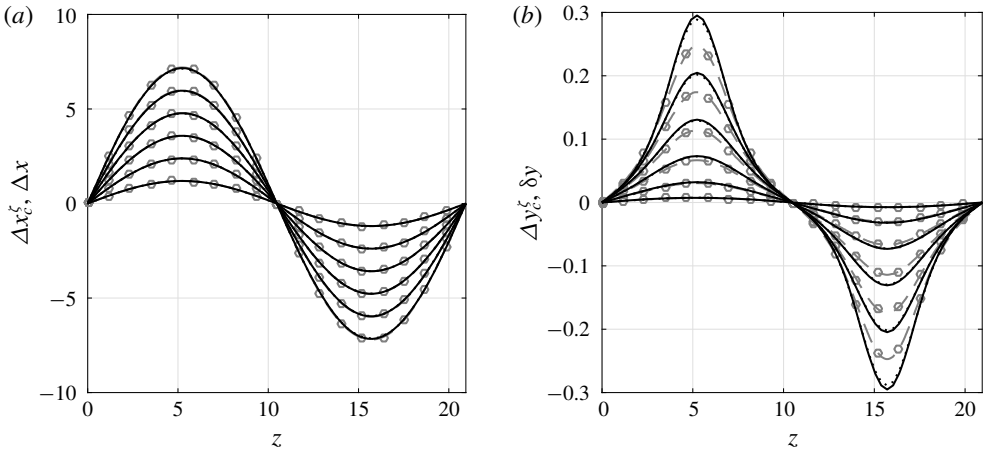


FIGURE 9. (*a*,*b*) Comparison between the vertical vorticity centroids Δx_c^ζ (*a*) and Δy_c^ζ (*b*) (grey dashed lines with open circles) and the asymptotic predictions for the displacements Δx and δy (black solid lines) as a function of z at different times $t = 6$, 12, 18, 24, 30, 36 (increasing amplitudes). The dotted lines represent the exact solution obtained by numerical integration of (4.3)–(4.4). The parameters are $F_h = 0.5$, $k_z = 0.3$, $U_S = 0.2$ and $Re = 6000$.

Figure 9 shows the vertical profiles of the x and y displacements at different times. As can be seen in figure 9(*a*), the agreement between the vertical vorticity centroid Δx_c^ζ measured in the simulations (grey dashed lines with open circles) and the asymptotic prediction Δx (black solid lines) is excellent along all the vertical. It follows very well the sinusoidal profile $\Delta x = U_s t \sin(k_z z)$ since the correction δx is much smaller. There is also a good agreement between the numerics and the asymptotics for the y-displacement (figure 9*b*) although some departures appear around the extrema for large time, as was already seen in figure 8(*b*). It is also clearly visible that the y-displacement departs from a sinusoidal shape as time increases. This non-sinusoidal profile comes from the vertical variations of the parameter $\mathcal{A}$ (in the second term of (4.6)) induced by the modulation of the angular velocity of the vortex along the vertical. We have also plotted in figure 9 the exact asymptotic displacements obtained by numerical integration of (4.3)–(4.4) (dotted lines). However, these curves are only visible around the maxima of δy at the latest time shown (figure 9*b*) because they are almost identical to the approximation (4.5)–(4.6).

We have also compared the vertical velocity field predicted by the asymptotics against its numerical counterpart. Figure 10 displays horizontal cross-sections of w in the plane $z = l_z/2$ where it is maximum. A very good qualitative and quantitative agreement is observed even at $t = 18$ (figure 10*c*,*f*) apart from the existence of small wave-like disturbances in the DNS that are absent in the asymptotics. The close agreement between the asymptotic and numerical results can be further seen in the temporal variations of the maximum values of w and b (figures 11*a* and 12*a*). The asymptotic and numerical results begin to slightly depart from each other as late as $t \simeq 10$. The maximum values of w and b increase initially linearly and then saturate with oscillations superimposed. These oscillations are due to the internal waves excited at $t = 0$. Two periods $T = 2\pi F_h = \pi$ and $T = 2\pi/\Omega(r = 0) = 2\pi$ are mixed, explaining why the oscillations look somewhat irregular, especially for w_m (figure 11*a*).

https://doi.org/10.1017/jfm.2020.227 Published online by Cambridge University Press

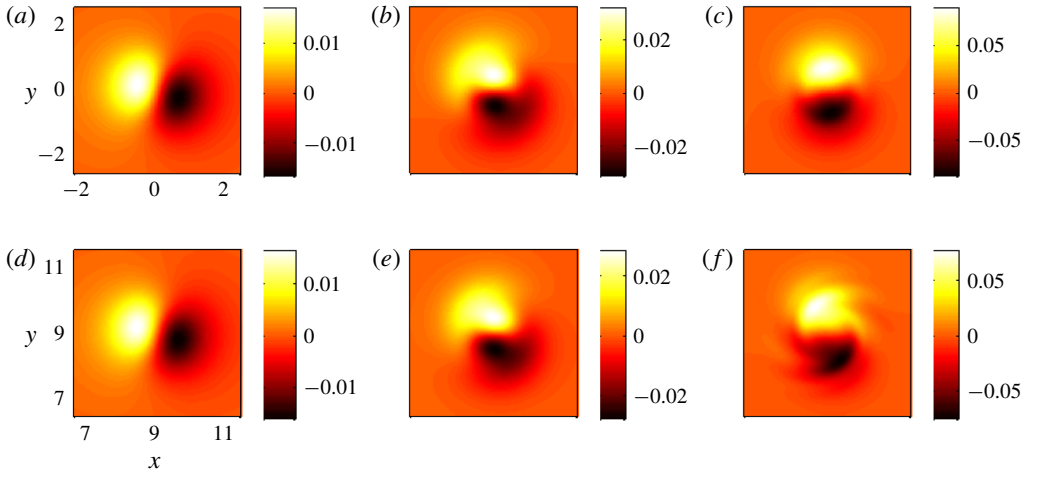


FIGURE 10. Horizontal cross-sections in the plane $z = l_z/2$ of (*a–c*) the vertical velocity calculated asymptotically and (*d–f*) in the DNS for $F_h = 0.5$, $k_z = 0.3$, $U_S = 0.2$ and $Re = 6000$ at $t = 2$ (*a*,*d*), $t = 6$ (*b*,*e*) and $t = 18$ (*c*,*f*).

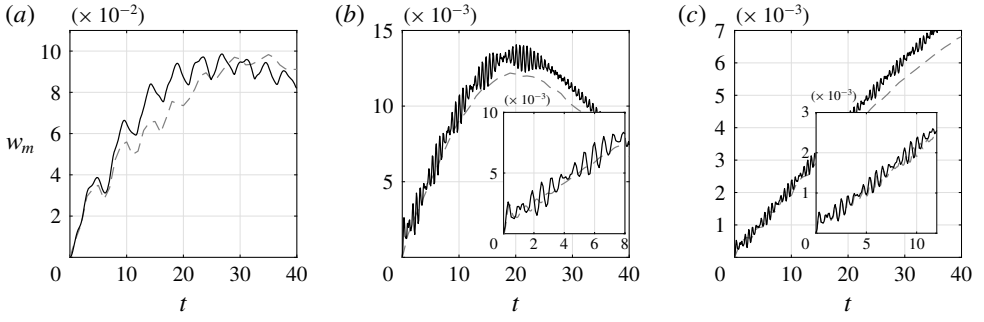


FIGURE 11. Evolution of the maximum velocity w_m in the plane $z = l_z/2$ in the DNS (grey dashed lines) and from the asymptotic predictions (black solid lines) for $Re = 6000$, $U_S = 0.2$ for (*a*) $F_h = 0.5$, $k_z = 0.3$, (*b*) $F_h = 0.1$, $k_z = 1.5$, (*c*) $F_h = 0.1$, $k_z = 0.3$. The insets in (*b*,*c*) display a close-up view of the initial evolution.

Similar agreements have been observed for different values of U_S and Re. In the next subsection, we investigate the effects of varying the Froude number and the wavenumber.

4.2.2. *Effects of F_h and k_z*

Figures 11(*b*,*c*) and 12(*b*,*c*) show the evolution of the maximum vertical velocity and buoyancy for a lower Froude number $F_h = 0.1$ and two different wavenumbers. In the first case (figures 11*b* and 12*b*), the wavenumber has been increased to $k_z = 1.5$ so that the product $k_z F_h = 0.15$ is the same as before while, in the second case (figures 11*c* and 12*c*), the wavenumber is still $k_z = 0.3$. The agreement is good for both wavenumbers confirming that the relevant small parameter is $k_z F_h$ and not k_z. However, we can notice that the oscillations of the maximum buoyancy are strongly reduced when $F_h = 0.1$ (figure 12*b*,*c*) compared to $F_h = 0.5$ (figure 12*a*). This is

https://doi.org/10.1017/jfm.2020.227 Published online by Cambridge University Press

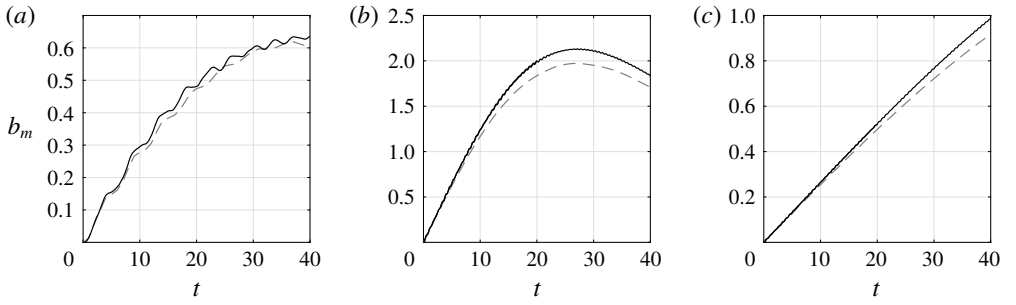


FIGURE 12. Evolution of the maximum buoyancy b_m in the plane $z = l_z/2$ in the DNS (grey dashed lines) and from the asymptotic predictions (black solid lines) for $Re = 6000$, $U_S = 0.2$ for (*a*) $F_h = 0.5$, $k_z = 0.3$, (*b*) $F_h = 0.1$, $k_z = 1.5$, (*c*) $F_h = 0.1$, $k_z = 0.3$.

because the amplitude of the internal waves in the buoyancy scales as the Froude number. In contrast, oscillations are still visible in the evolution of the maximum asymptotic vertical velocity for $F_h = 0.1$ (figure 11*b*,*c*) since the amplitude of the internal waves in this field does not vanish in the limit of small Froude number. However, no oscillations are present at large time in the DNS (dashed lines) for $F_h = 0.1$ unlike for $F_h = 0.5$ (figure 11). Nevertheless, the mean evolution of w_m in the DNS is close to the one predicted by the asymptotics for $F_h = 0.1$. The insets in figure 11(*b*,*c*) show a close-up view of the initial evolution of w_m for $F_h = 0.1$. We can see that the oscillations are quickly damped in the DNS for $k_z = 1.5$ (figure 11*b*) and disappear for $t \gtrsim 3$. For $k_z = 0.3$ (figure 11*c*), they persist for a longer time and start to decay only after $t \sim 10$. For $t < 10$ the agreement between the asymptotics and the numerics is excellent.

The reason for these discrepancies is the following. As already mentioned, the asymptotic problem has been solved in Part 1 for long wavelengths by assuming $k_z F_h \ll 1$. The reason why $k_z F_h$ is the appropriate parameter is that the buoyancy length scale is the natural vertical length scale of vortical motions in strongly stratified inviscid flows (Billant & Chomaz 2001). However, this self-similarity does not apply to the internal waves that are generated at the start-up of the motion because they evolve on the fast time scale $1/F_h$ and not on the turnover time scale of the vortex. For this reason, the asymptotic calculation of the internal waves component performed in Part 1 is actually correct only when k_z is small but not if k_z is of order unity and F_h small. For finite k_z, the internal waves could be computed only numerically. However, the inset in figure 11(*b*) shows that only few oscillation cycles are present at the beginning. This is because the internal waves quickly propagate away from the vortex core. Indeed, their radial group velocity, which is proportional to k_z^2/F_h, is large for $k_z = O(1)$ and $F_h \ll 1$. In contrast, when k_z is small and F_h finite, the radial group velocity is small, meaning that the internal waves remain a long time in the vortex core, i.e. are almost purely standing waves as found in the asymptotic analysis. This is the reason why the oscillation cycles are seen for a longer time for $k_z = 0.3$ (inset in figure 11*c*) than for $k_z = 1.5$ (inset in figure 11*b*).

Since finite k_z will be mostly considered in the following, we have chosen to completely neglect the internal waves for these reasons.

https://doi.org/10.1017/jfm.2020.227 Published online by Cambridge University Press

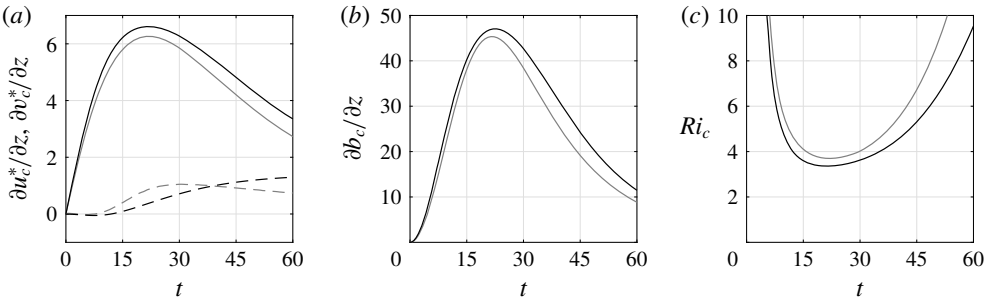


FIGURE 13. Evolution of (*a*) $\partial u^*/\partial z$ (dashed line), $\partial v^*/\partial z$ (solid line), (*b*) $\partial b/\partial z$ and (*c*) Ri at $\tilde{r}=0$, $z=l_z/2$ from the DNS (grey lines) and predicted from the asymptotics (black lines). The parameters are $F_h=0.1$, $k_z=\pi$, $U_S=0.2$, $Re=6000$.

4.3. *Evolution of the vertical shear and the Richardson number*

We now investigate the evolution of the flow at the vortex centre and at the level $z=l_z/2$ where the ambient shear is maximum. As seen in § 3, this is the location (together with the symmetric point $z=0$) where the Richardson number reaches its minimum or where the Kelvin–Helmholtz instability first appears.

Figure 13(*a*,*b*) compares $\partial u^*/\partial z$, $\partial v^*/\partial z$ and $\partial b/\partial z$ at the vortex centre at $z=l_z/2$ observed in the DNS for $F_h=0.1$, $k_z=\pi$, $U_S=0.2$ and $Re=6000$ (grey lines) to their asymptotic counterparts derived in Part 1 (black lines). Apart from $\partial u_c^*/\partial z$, the agreement is very good over the entire time range investigated. Since $\partial v_c^*/\partial z$ and $\partial b_c/\partial z$ depend only on the quantity $t\Omega_c$ at leading order in k_zF_h (where Ω_c is the angular velocity at $\tilde{r}=0$, $z=l_z/2$), this agreement is an indirect confirmation of the relation (4.8) for the angular velocity at the vortex centre. The magnitude of $\partial u_c^*/\partial z$ is much lower than for $\partial v_c^*/\partial z$. The beginning of its evolution is well predicted by the asymptotics until $t\simeq 5-10$ but not later. Several checks led us to the conclusion that this discrepancy is not due to an error in our calculations but is most probably due to higher-order effects, not considered in the asymptotic analysis, that become quickly dominant over the leading order when $k_zF_hU_St>1$. This is because the asymptotic expansion is not uniformly asymptotic in time since the long-wavelength assumption is expected to be no longer valid when $k_zF_hU_St>1$ because vertical gradients grow like k_zU_St. Nevertheless, figure 13(*a*,*b*) shows that the asymptotics for $\partial v_c^*/\partial z$ and $\partial b_c/\partial z$ remain in good agreement even when $t=60$, i.e. $k_zF_hU_St\sim 4$. Despite this discrepancy on $\partial u_c^*/\partial z$, figure 13(*c*) shows that the asymptotic Richardson number Ri_c is in good agreement with the one computed from the DNS since $\partial u_c^*/\partial z$ is one order smaller in $(k_zF_h)^2$ than $\partial v_c^*/\partial z$ and $\partial b_c/\partial z$.

The main assumption of the long-wavelength asymptotic analysis, i.e. $k_zF_h\ll 1$, is reasonably well satisfied for the parameters of figure 13 since $k_zF_h=0.31$. Figure 14 further compares the evolutions of $\partial u_c^*/\partial z$, $\partial v_c^*/\partial z$, $\partial b_c/\partial z$ and Ri_c when F_h or k_z are increased. Surprisingly, the agreement between the asymptotics and numerics for $\partial v_c^*/\partial z$ and $\partial b_c/\partial z$ remains satisfactory even if k_zF_h has been increased up to unity. Regarding $\partial u_c^*/\partial z$ (figure 14*a*), a large discrepancy is always observed like in figure 13(*a*). When F_h is increased from $F_h=0.1$ (dashed-dotted lines) to $F_h=0.5$ (solid lines), keeping the wavenumber constant $k_z=2$, $\partial v_c^*/\partial z$ and $\partial b_c/\partial z$ decrease (figure 14*b*,*c*) while $\partial u_c^*/\partial z$ increases (figure 14*a*). The maxima of $\partial u_c^*/\partial z$ and $\partial v_c^*/\partial z$ become even of the same magnitude for $F_h=0.5$, in sharp contrast to what

https://doi.org/10.1017/jfm.2020.227 Published online by Cambridge University Press

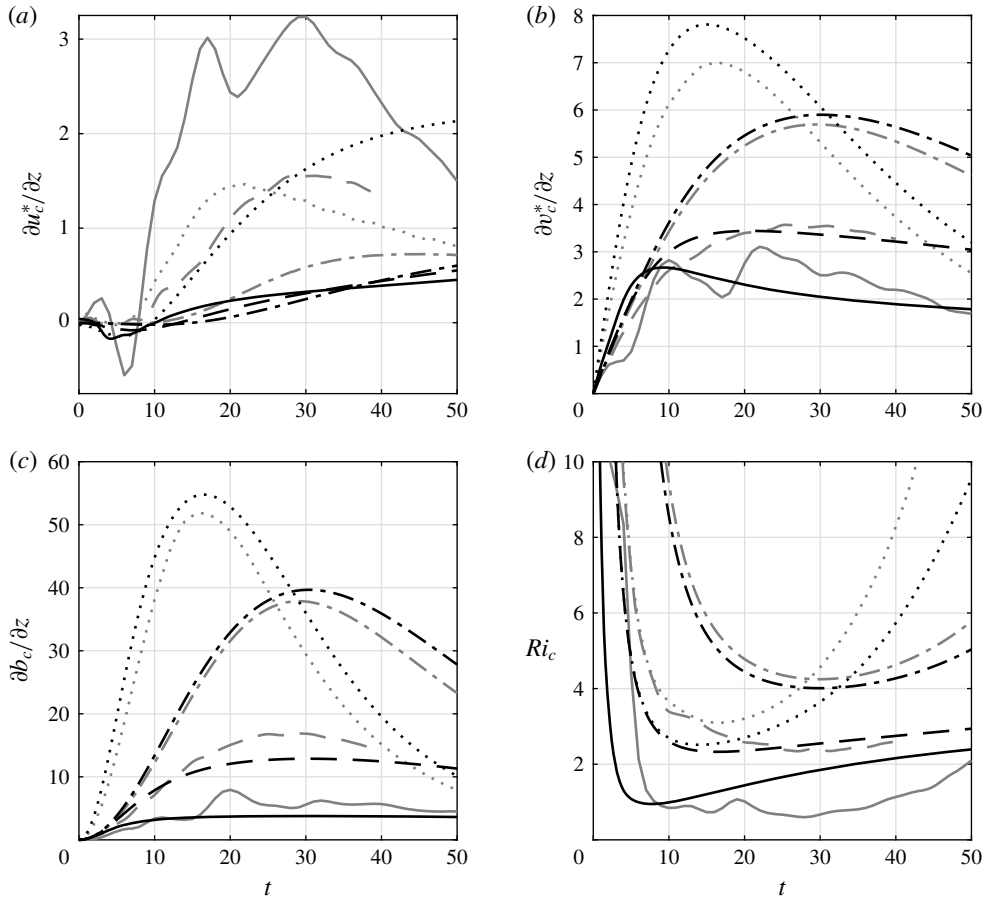


FIGURE 14. Evolution of (*a*) $\partial u^*/\partial z$, (*b*) $\partial v^*/\partial z$, (*c*) $\partial b/\partial z$ and (*d*) Ri at $\tilde{r}=0$, $z=l_z/2$, for $U_S=0.2$, $Re=6000$, for ($F_h=0.1$, $k_z=2$) (dash-dotted lines), ($F_h=0.25$, $k_z=2$) (dashed lines), ($F_h=0.5$, $k_z=2$) (solid lines) and ($F_h=0.1$, $k_z=5$) (dotted lines) from the DNS (grey lines) and predicted by the asymptotics (black lines).

was observed in figure 13. Large oscillations are present in the DNS for $F_h=0.5$ (figure 14). We have checked that they are not due to the internal waves that have been neglected in the asymptotics. They seem rather related to some vortex waves since $\partial u_c^*/\partial z$ and $\partial v_c^*/\partial z$ oscillate out of phase, as also observed in figure 5(*b*).

In contrast, when k_z is increased from $k_z=2$ (dashed-dotted lines in figure 14) to $k_z=5$ (dotted lines) keeping the Froude number constant $F_h=0.1$, the vertical shear and the buoyancy vertical gradient saturate earlier and at higher levels.

The minimum of the Richardson number decreases as k_z or F_h increases (figure 14*d*). The asymptotic and numerical Richardson numbers remain in rough agreement even for $F_h=0.5$ (solid lines) despite the large increase of $\partial u_c^*/\partial z$ as F_h increases. In particular, the minimum values are $\min(Ri_c)\simeq 0.95$ and $\min(Ri_c)\simeq 0.6$, respectively. The minimum of the asymptotic Richardson number is lower than the bound $\min(Ri_c)>3.43$ derived in Part 1 for $k_zF_h\ll 1$ since $k_zF_h=O(1)$. We can notice that the beginning of the evolution of the Richardson number for ($F_h=0.25$, $k_z=2$) (dashed lines) is similar to the one for ($F_h=0.1$, $k_z=5$) (dotted lines) (figure 14*d*)

https://doi.org/10.1017/jfm.2020.227 Published online by Cambridge University Press

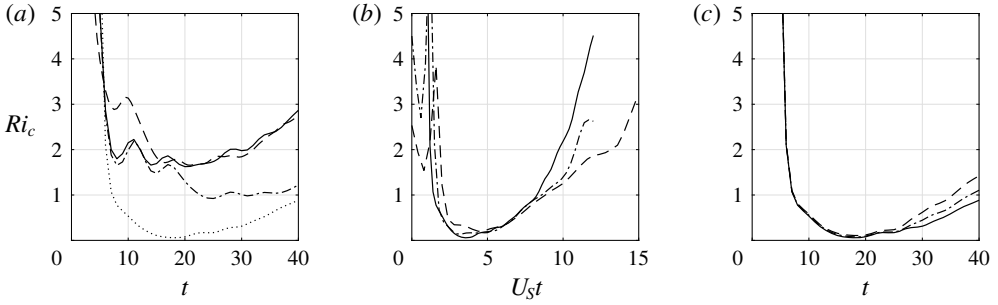


FIGURE 15. Evolution of the Richardson number at the vortex centre at $z = l_z/2$ for $U_S = 0.2$ and for (*a*) $k_z = \pi/2$, $F_h = 0.5$, $Re = 1500$ (solid line), $k_z = \pi/2$, $F_h = 0.5$, $Re = 6000$ (dash-dotted line), $k_z = \pi$, $F_h = 0.25$, $Re = 6000$ (dashed line), $k_z = \pi$, $F_h = 0.5$, $Re = 6000$ (dotted line). (*b*) Ri_c as a function of $U_S t$ for $Re = 6000$, $k_z = \pi$, $F_h = 0.5$ and $U_S = 0.2$ (solid line), $U_S = 0.3$ (dash-dotted line) and $U_S = 0.4$ (dashed line). (*c*) Ri_c as a function of t for $k_z = \pi$, $F_h = 0.5$, $U_S = 0.2$ and $Re = 6000$ (solid line), $Re = 5000$ (dash-dotted line) and $Re = 4000$ (dashed line).

since $k_z F_h = 0.5$ in both cases. The subsequent evolutions differ because the buoyancy Reynolds numbers are different: $Re_b = 1500$ and $Re_b = 60$, respectively.

Similar agreements have been observed for other values of U_S and Re.

5. Evolution of the Richardson number for finite $k_z F_h$

In this section, we now study the regime of finite $k_z F_h$ mainly based on the DNS since the long-wavelength analysis is *a priori* no longer expected to be valid. Figure 15(*a*) displays the evolution of the Richardson number in the DNS at the vortex centre at $z = l_z/2$ for four particular combinations of the parameters (k_z, F_h, Re). It is interesting to compare two curves at a time. First, the solid and dashed lines correspond to different Froude numbers $F_h = 0.5$ and $F_h = 0.25$, respectively, but with the same values of the rescaled wavenumber $k_z F_h = \pi/4$ and of the buoyancy Reynolds number $ReF_h^2 = 375$. These two curves superpose quite well apart from the oscillations. Similarly, the dashed and dashed dotted lines share the same values of $k_z F_h = \pi/4$ and of Reynolds number $Re = 6000$ but have a different buoyancy Reynolds number. In this case, the evolutions of Ri_c differ. Finally, the dashed and dotted lines have the same wavenumber $k_z = \pi$ and Reynolds number $Re = 6000$ but different Froude numbers. In this case also, the evolution of Ri_c differs widely as already seen before in figure 14. Altogether, this demonstrates that Ri_c depends mainly on (k_z, F_h, Re) only through the two parameters $k_z F_h$ and ReF_h^2. The same conclusion can be drawn from other sets of parameters.

Similarly, figure 15(*b*) shows the evolution of Ri_c for different values of U_S for $k_z = \pi$, $F_h = 0.5$, $Re = 6000$. The time has been rescaled by U_S in this case. The different curves are very close to each other, indicating that U_S has only a weak effect on the Richardson number. Finally, figure 15(*c*) shows that the Reynolds number has only a small influence on the evolution of Ri_c when it is sufficiently large and when the other parameters are kept constant.

The minimum value of the Richardson number $\min(Ri_c)$ reached in most of the DNS is further summarized in figure 16 as a function of the three main parameters: $k_z F_h$, U_S and ReF_h^2. A filled symbol is used when the shear instability is observed

https://doi.org/10.1017/jfm.2020.227 Published online by Cambridge University Press

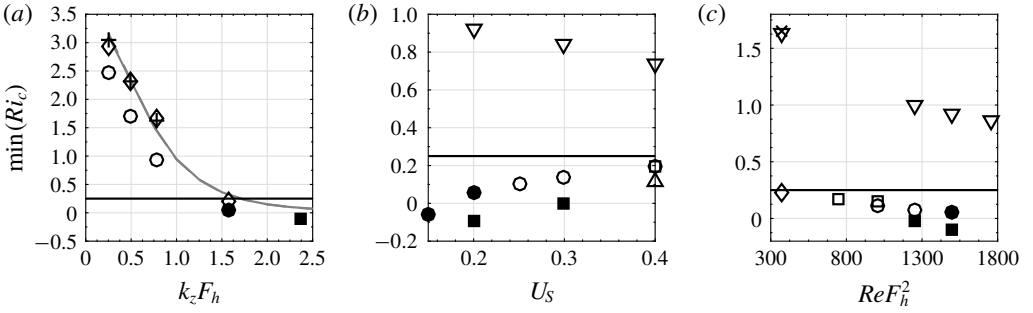


FIGURE 16. Minimum Richardson number in numerical simulations (symbols) at the vortex centre at $z = l_z/2$ as a function of (*a*) k_zF_h, (*b*) U_S and (*c*) ReF_h^2. The different symbols/lines correspond to (*a*): $F_h = 0.5$, $Re = 6000$ (circles), $F_h = 0.25$, $Re = 6000$ (diamonds), $F_h = 0.5$, $Re = 1500$ (plus sign) for $U_S = 0.2$; (*b*): $F_hk_z = \pi/4$ (downward triangle), $F_hk_z = \pi/2$ (circles), $F_hk_z = 3\pi/4$ (squares) and $F_hk_z = \pi$ (upward triangle) for $F_h = 0.5$, $Re = 6000$; (*c*): $F_hk_z = \pi/4$, $F_h = 0.5$ (downward triangle), $F_hk_z = \pi/4$, $F_h = 0.25$ (cross), $F_hk_z = \pi/2$, $F_h = 0.5$ (circles), $F_hk_z = \pi/2$, $F_h = 0.25$ (diamonds) and $F_hk_z = 3\pi/4$, $F_h = 0.5$ (squares) for $U_S = 0.2$. Filled and empty symbols correspond to runs where the shear instability develops or not, respectively. The grey lines in (*a*) represent the asymptotic predictions for $F_h = 0.5$ (solid line) and $F_h = 0.25$ (dashed line) for $Re = 6000$, $U_S = 0.2$ (they are indistinguishable). The horizontal solid lines indicate the threshold $\min(Ri_c) = 1/4$.

and an open symbol, otherwise. When the shear instability develops, the minimum Richardson number is then generally negative owing to the overturnings induced by the instability. However, this negative value has no particular meaning except the fact that it is below the threshold 1/4. As seen in figure 16(*a*), $\min(Ri_c)$ decreases with k_zF_h and goes below 1/4 when $k_zF_h \gtrsim 1.6$ for both $F_h = 0.25$ (diamonds) and $F_h = 0.5$ (circles) for $Re = 6000$. However, the shear instability has been observed only for $F_h = 0.5$. For $F_h = 0.25$, the minimum Richardson number is just below 1/4: $\min(Ri_c) = 0.2$ for the highest wavenumber that has been investigated $k_zF_h = 1.6$. It is likely that the shear instability would be also triggered for $F_h = 0.25$ if a larger value of k_zF_h were investigated. As shown previously, the differences between the minimum Richardson number for $F_h = 0.25$ and $F_h = 0.5$ are due to the difference in buoyancy Reynolds number $Re_b = ReF_h^2$. Indeed, the symbols plus, corresponding also to $F_h = 0.5$ but with the lower Reynolds number $Re = 1500$, are almost superposed on those for $F_h = 0.25$, $Re = 6000$ which have the same buoyancy Reynolds number. Remarkably, the dependence of $\min(Ri_c)$ with k_zF_h is well reproduced by the asymptotics (lines) even if the time evolution of Ri_c differs in the numerics and the asymptotics for $k_zF_h = O(1)$ (figure 14). In particular, the asymptotic minimum Richardson number goes below 1/4 when $k_zF_h \gtrsim 1.7$ almost independently of F_h, U_S and for a wide range of Re.

Figure 16(*b*) shows that $\min(Ri_c)$ increases slightly with U_S for $k_zF_h = \pi/2$ and $k_zF_h = 3\pi/4$ but decreases when $k_zF_h = \pi/4$ for $F_h = 0.5$ and $Re = 6000$. For $k_zF_h = \pi/2$ and $F_hk_z = 3\pi/4$, $\min(Ri_c)$ is always below 1/4 but the shear instability develops only if $\min(Ri_c)$ is sufficiently smaller than this threshold. It has been observed for $U_S = 0.2$ for both $k_zF_h = \pi/2$ and $k_zF_h = 3\pi/4$. In contrast, for $U_S = 0.3$, the shear instability occurs when $k_zF_h = 3\pi/4$ but not for $k_zF_h = \pi/2$ while for $U_S = 0.4$, no instability has been observed for both wavenumbers. An additional simulation for $U_S = 0.4$, $F_h = 0.5$ at higher k_zF_h: $k_zF_h = \pi$, still does not exhibit the shear instability even if

https://doi.org/10.1017/jfm.2020.227 Published online by Cambridge University Press

$\min(Ri_c)$ is well below 1/4: $\min(Ri_c) = 0.11$. The development of the shear instability could be less favoured as U_S increases because the time interval Δt during which $\min(Ri_c)$ is below 1/4 becomes shorter. Indeed, figure 15(*b*) shows that the evolution of Ri_c is almost independent of U_S when represented as a function of $U_S t$, implying that Δt decreases with U_S. Thus, the shear instability has less time to develop for large U_S if its growth rate is assumed to be independent of U_S.

The minimum Richardson number also decreases slightly as the buoyancy Reynolds number increases (figure 16*c*). Hence, the shear instability develops only for sufficiently high Reynolds number: when $ReF_h^2 \geqslant 1500$ for $k_z F_h = \pi/2$ and when $ReFh^2 \geqslant 1250$ for $k_z F_h = 3\pi/4$. In addition to the slight decrease of $\min(Ri_c)$ as the buoyancy Reynolds number increases, the lower viscous damping should also favour the growth of the shear instability.

6. Conclusion

We have performed direct numerical simulations of the evolution of an initially columnar vortex in an ambient shear flow in a strongly stratified fluid. The numerical results have been compared to the asymptotic analysis carried out in Part 1.

The DNS show that the vortex is progressively bent in the direction of the shear flow but is also deviating in the orthogonal direction. The decay of its potential vorticity is enhanced in the regions of high shear. For $k_z F_h \gtrsim 1.6$ and sufficiently high buoyancy Reynolds number ReF_h^2, the Kelvin–Helmholtz instability is first triggered in the centre of the vortex at the vertical levels where the ambient vertical shear is maximum, i.e. $z = 0$, $l_z/2$. For the other parameters for which the shear instability does not develop, the Richardson number reaches its minimum at the same locations. We have therefore concentrated our efforts on a comparison of the evolution of the flow at this location to the predictions of the long-wavelength asymptotic analysis performed for $k_z F_h \ll 1$ in Part 1.

For sufficiently small $k_z F_h$, the long-wavelength asymptotic analysis turns out to predict accurately the deformations of the vortex axis, as well as the evolution of the vertical shear of the vortex in the spanwise direction $\partial v_c^*/\partial z$ and of the vertical gradient of the buoyancy $\partial b_c/\partial z$ at the vortex centre at $z = l_z/2$. The prediction for the streamwise shear of the vortex $\partial u_c^*/\partial z$ is not accurate but this is not dramatic since it is one order smaller in $(k_z F_h)^2$ than $\partial v_c^*/\partial z$ and $\partial b_c/\partial z$. Hence, the Richardson number at the vortex centre and $z = l_z/2$ based on these asymptotic expressions is in good agreement with the DNS provided that $k_z F_h$ is small.

From the numerical simulations, we have found that the minimum Richardson number in the centre of the vortex at $z = l_z/2$ goes below 1/4 only when $k_z F_h$ is finite: $k_z F_h \gtrsim 1.6$. Remarkably, this threshold agrees with that predicted by the asymptotics $k_z F_h \gtrsim 1.7$ even if it is beyond its range of validity ($k_z F_h \ll 1$). Nevertheless, the shear instability develops only if the minimum Richardson number is sufficiently smaller than 1/4. In addition, the buoyancy Reynolds number has to be sufficiently large. Decreasing the velocity of the shear flow tends also to favour the shear instability.

In summary, the conditions for the development of the Kelvin–Helmholtz instability when a two-dimensional vortex is subjected to an external stratified shear flow depend mostly on the intensity of the vortex itself $\Gamma/(2\pi a_0^2)$ and little on the dimensional amplitude $\hat{U}_S$ of the shear flow. Indeed, the minimum Richardson number of the shear flow $Ri_s = N^2/(\hat{k}_z \hat{U}_S)^2$ can be arbitrarily large. In this sense, the ambient shear flow can be seen as only a catalyst. Nevertheless, the dimensional wavenumber $\hat{k}_z$ of the shear flow has to satisfy the condition $\hat{k}_z a_0 F_h \gtrsim O(1)$. This condition ensures that the

https://doi.org/10.1017/jfm.2020.227 Published online by Cambridge University Press

typical order of magnitude of the Richardson number when the vortex will be bent over the vertical length scale $2\pi/\hat{k}_z$, i.e. $Ri \sim N^2/(\hat{k}_z\Gamma/(2\pi a_0^2))^2 = 1/(\hat{k}_z a_0 F_h)^2$, will be lower than unity.

We can try to extrapolate these results to stratified turbulence forced two-dimensionally in the horizontal plane (Waite & Bartello 2004; Lindborg 2006; Brethouwer *et al.* 2007; Augier *et al.* 2014; Augier, Billant & Chomaz 2015). Indeed, in this case, columnar structures are continuously generated by the forcing within a pre-existing turbulence with a layered structure. Such structure is likely to contain shear flows with the same vertical length scale. Since the vertical length scale of the layers typically scales as the buoyancy length scale $L_v \sim F_h L_h$, we should have $2\pi L_h/L_v F_h \sim O(1)$, i.e. the condition $k_z F_h \gtrsim O(1)$ should be met. Therefore, as soon as they are generated by the forcing, columnar structures may be destabilized into small scales by the shear instability. It is worth pointing out that this process may occur even if the magnitudes of the shear flow components are small since we have seen that the dynamics in the case of a single vortex depends weakly on U_S. This also suggests that the so-called shear modes often present in numerical simulations of stratified turbulence (Lindborg 2006; Augier *et al.* 2015) may have an important effect even if they are weak.

In the future, it would be interesting to consider the additional effect of a Coriolis force in order to better understand the effect of an ambient shear flow on cyclones and more generally on geophysical vortices.

Acknowledgements

We thank D. Guy and V. Toai for technical assistance, and I. Delbende, F. Godeferd, S. Le Dizès, L. Oruba, R. Plougonven and the referees for helpful comments. This work was granted access to the HPC resources of IDRIS under the allocation 2016-A0062A07419 attributed by GENCI (Grand Equipement National de Calcul Intensif).

Declaration of interests

The authors report no conflict of interest.

REFERENCES

AUGIER, P. & BILLANT, P. 2011 Onset of secondary instabilities on the zigzag instability in stratified fluids. *J. Fluid Mech.* **682**, 120–131.

AUGIER, P., BILLANT, P. & CHOMAZ, J.-M. 2015 Stratified turbulence forced with columnar dipoles: numerical study. *J. Fluid Mech.* **769**, 403–443.

AUGIER, P., BILLANT, P., NEGRETTI, M. E. & CHOMAZ, J.-M. 2014 Experimental study of stratified turbulence forced with columnar dipoles. *Phys. Fluids* **26**, 046603.

AUGIER, P., CHOMAZ, J.-M. & BILLANT, P. 2012 Spectral analysis of the transition to turbulence from a dipole in stratified fluid. *J. Fluid Mech.* **713**, 86–108.

BILLANT, P. & CHOMAZ, J.-M. 2001 Self-similarity of strongly stratified inviscid flows. *Phys. Fluids* **13**, 1645–1651.

BONNICI, J. 2018 Décorrélation verticale d'un tourbillon soumis à un champ de cisaillement dans un fluide fortement stratifié. PhD thesis, LadHyX, Université Paris-Saclay.

BONNICI, J. & BILLANT, P. 2020 Evolution of a vortex in a strongly stratified shear flow. Part 1: Asymptotic analysis. *J. Fluid Mech.* **893**, A17.

BRETHOUWER, G., BILLANT, P., LINDBORG, E. & CHOMAZ, J.-M. 2007 Scaling analysis and simulation of strongly stratified turbulent flows. *J. Fluid Mech.* **585**, 343–368.

https://doi.org/10.1017/jfm.2020.227 Published online by Cambridge University Press

DELONCLE, A., BILLANT, P. & CHOMAZ, J.-M. 2008 Nonlinear evolution of the zigzag instability in stratified fluids : a shortcut on the route to dissipation. *J. Fluid Mech.* **599**, 299–239.

HOWARD, L. N. 1961 Note on a paper of John W. Miles. *J. Fluid Mech.* **10**, 509–512.

LAVAL, J.-P., MCWILLIAMS, J. C. & DUBRULLE, B. 2003 Forced stratified turbulence: successive transitions with Reynolds number. *Phys. Rev.* E **68** (3), 036308.

LILLY, D. K. 1983 Stratified turbulence and the mesoscale variability of the atmosphere. *J. Atmos. Sci.* **40**, 749–761.

LINDBORG, E. 2006 The energy cascade in a strongly stratified fluid. *J. Fluid Mech.* **550**, 207–242.

MILES, J. W. 1961 On the stability of heterogeneous shear flows. *J. Fluid Mech.* **10**, 496–508.

OTHEGUY, P., CHOMAZ, J.-M. & BILLANT, P. 2006 Elliptic and zigzag instabilities on co-rotating vertical vortices in a stratified fluid. *J. Fluid Mech.* **553**, 253–272.

PRADEEP, D. S. & HUSSAIN, F. 2004 Effects of boundary condition in numerical simulations of vortex dynamics. *J. Fluid Mech.* **516**, 115–124.

RENNICH, S. C. & LELE, S. K. 1997 Numerical method for incompressible vortical flows with two unbounded directions. *J. Comput. Phys.* **137** (1), 101–129.

RILEY, J. J. & DEBRUYNKOPS, S. M. 2003 Dynamics of turbulence strongly influenced by buoyancy. *Phys. Fluids* **15**, 2047–2059.

WAITE, M. L. 2013 The vortex instability pathway in stratified turbulence. *J. Fluid Mech.* **716**, 1–4.

WAITE, M. L. & BARTELLO, P. 2004 Stratified turbulence dominated by vortical motion. *J. Fluid Mech.* **517**, 281–308.

WAITE, M. L. & SMOLARKIEWICZ, P. K. 2008 Instability and breakdown of a vertical vortex pair in a strongly stratified fluid. *J. Fluid Mech.* **606**, 239–273.

https://doi.org/10.1017/jfm.2020.227 Published online by Cambridge University Press